Dalton Transactions

Accepted Manuscript

ROYAL SOCIETY OF CHEMISTRY

www.rsc.org/dalton

Graphical Abstract

Warm white light generation through modification in CCT by incorporation of defect level induced emission of ZnO in $Y_{1.993}Dy_{0.001}Tm_{0.006}O_3$ nano-phosphor

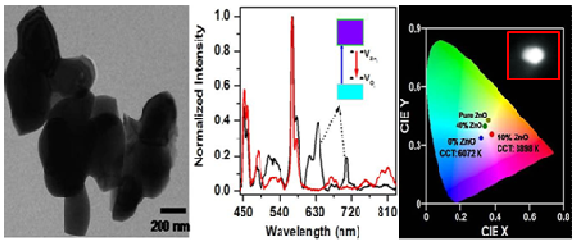

Probing a new approach for warm white light generation in lanthanide doped nanophosphors

M. Rai,[a] G. Kaur,[a] S. K. Singh,*[,b] S. B. Rai*[,a]

[a]Department of Physics, Banaras Hindu University, Varanasi-221005, India

[b]Department of Physics, Indian Institute of Technology (Banaras Hindu University), Varanasi-221005, India

*Corresponding authors:

Email: sunilcfsl@gmail.com (S. K. Singh), sbrai49@yahoo.co.in (S. B. Rai)

Tel.: *+91 542 230 7308;* ***fax:*** *+91 542 236 9889.*

Abstract

Lanthanides are among one of the most acceptable activator ions for cool white light emission; however, solid state lighting for several applications demands essentially a warm white light. Herein, present work probes a new approach for color temperature tuning in such systems to get a warm white light. Idea is that, the additional use of red spectral component in cool white light, to a certain extent, may lead to a perfect warm white light, which can be set off by making use of the surface oxygen defects mediated red emission from ZnO. To realize this noble concept, initially white light has been produced in $Y_{1.993}Dy_{0.001}Tm_{0.006}O_3$ and further ZnO has been added. Study includes detailed structural, optical (steady state and time domain), chromaticity coordinate (CIE) calculation and correlated color temperature (CCT) analysis. Results depicts that, initially, at low ZnO concentration, Zn^{2+} ions prefer to go into the interstitial sites, due to mismatch of ionic radius of Y^{3+} (0.90 Å) and Zn^{2+} (0.75 Å). However, beyond 10 mol% concentration of ZnO, solubility limit of Zn^{2+} ion in the Y_2O_3 matrix is attained, which results in the development of Y_2O_3-ZnO composite. The presence of ZnO phase give rise to defect level induced red emission, in addition, which tunes the color temperature from 6072 K to 3898 K, which is reasonably good warm white light for solid state lighting application. The idea can be generalized in other similar hosts also for developing potential warm white light sources.

Keywords: Lanthanide, nanophosphor, photoluminescence, white light, Zinc oxide

1. Introduction

Recently, inorganic white light emitting phosphors have emerged as novel and adequate fluorescent materials for lighting applications.[1-4] A typical approach for commercial application involves a combination of NUV light emanated by an AlGaN chip coated with the phosphor layer.[5,6] However, in spite of pertinent improvements, it still doesn't meet the ideal necessities of a warm white light source characterized by correlated color temperature CCT< 4000 K.[7] The other alternative is to fabricate multi-phosphor systems; which is, relatively less attractive, because such systems face serious problem of re-absorption of emission, and moreover to this, a difference in the degradation rate of individual phosphor limit their performances as well. Thus, it remains imperative to concentrate on a sole composition phosphor.[8-11]

A considerable effort has been imposed to get white light emission in a sole matrix, mostly through lanthanide ion co-doping. Lanthanide doped white light phosphors may be classified into three sorts. The first one is based on the broad band emission from lanthanide (e.g. Eu^{2+}, Mn^{2+}) and co-dopant ions, covering entire visible region. This methodology to a great extent relies upon host matrix and the environment around emitting ion. Accordingly, it obliges an extremely controlled synthesis mechanism so as to maintain a similar host-guest interaction, defect level (DL) formation, and homogeneity in the system, etc. for reproducibility, which is often a tedious task.[12] Another common approach is the mixing of red, green and blue (RGB) colors, emanated by three different lanthanide ions. Herein, again, tuning the ratio of three ions is a cumbersome process. So, in the third approach, mixing of blue and yellow colors is adopted, which requires two lanthanide ions only. One such popular combination is Tm^{3+} and Dy^{3+}. The hypersensitive transition $^4F_{9/2}\rightarrow{}^6H_{13/2}$ in yellow region by Dy^{3+} ion and blue transition $^1D_2\rightarrow{}^3F_4$ due to Tm^{3+} ions gives collectively a white light emission under UV excitation and referred as dichromatic

(*or di-band*) emission due to two spectral components.[12-15] Regardless, an acceptable color temperature still remains to attain for satisfactory warm white light.

This work puts forward a new approach for the color temperature tuning of white light emission in such systems so as to get an acceptable warm white light. It has been realized that the white light produced by Tm^{3+}, Dy^{3+} combination lacks red spectral component to produce a perfect warm white light. Authors suggest the additional use of ZnO to complement this lack of red spectral component, which can tune the color temperature to get a warm white light. Surface oxygen defects in ZnO are well known to give red spectral component.[16,17] The two main factors contributing to crystal defect are chemical imperfection and atomic arrangement. In such ZnO based phosphor composites, heat treatment/post annealing of as-synthesized phosphor/composite in ambient environment relaxes stress and vacancies in the lattice are trapped inside when the sample is cooled down to room temperature. This process effectively reduces the number of grains and so particles agglomerate resulting in more defect states with trapped oxygen in excess.[18]

To realize this noble concept, a well established commercially used host Y_2O_3 has been selected and then a nanocomposite of this host has been formed with varying concentration of ZnO. The material has been synthesized through a low temperature solution combustion route. Initially at low concentration of ZnO, Zn^{2+} occupies the interstitial position in yttria lattice and no appreciable change in color temperature is seen. However, beyond a certain concentration, the dissolution limit of ZnO in yttria matrix is reached and the phase due to ZnO itself also appears, making the system a composite material. Thus, evolution of red spectral content due to ZnO defect states tunes the color temperature, to below 4000 K, appreciably. A detailed structure (phase, particle size and microstructure), UV-Visible absorption, photoluminescence (steady

state and time domain), CIE color coordinate calculation, and color temperature tunability based on CCT studies has been performed and analyzed.

2. Experimental

2.1 Materials and Methods

Analytical reagent grade Y_2O_3 (Himedia, 99.99%), Dy_2O_3 (Loba Chemie, 99.9%), Tm_2O_3 (Alfa Aesar, 99.9%), ZnO (May & Baker LTD, 99%) were used as precursors, while urea was used as fuel. Nitrates of the oxides were prepared by dissolving them in HNO_3. Initially the concentration of Dy^{3+} was optimized (x = 0.1 mol %), and then Tm^{3+} ions were doped in different concentration (y = 0.0 to 0.8 mol%, in steps of 0.2) to find out an adequate composition for white light emission, which is 0.1 mol % Dy^{3+} and 0.6 mol % Tm^{3+} written as $Y_{1.993}Dy_{0.001}Tm_{0.006}O_3$. Further, different concentration of ZnO (0 to 40 mol %) was doped in the yttria matrix to form the composite material. $Y_{1.993}Dy_{0.001}Tm_{0.006}O_3$ doped ZnO sample has also been prepared. The synthesis was carried out using solution combustion technique, as reported in detail in our earlier works.[19] The mixture of nitrates and urea was stirred in a beaker to get a homogeneous transparent solution, which is then heated at 60 ^oC until a transparent gel is obtained. The gel kept in alumina crucible was allowed for auto ignition inside a close furnace maintained at 600 ^oC which resulted in foam like ceramic. The obtained phosphor samples were finally grinded to fine powder, and post annealed at 1200 ^oC for 2 h.

2.2 Instrumentation

X-ray diffraction (XRD) pattern was recorded by an 18 kW rotating anode (Cu k_α) based Rigaku powder diffractometer. Data were obtained from 2θ = 20° to 80° at a scanning speed of 3°/ minute. Transmission electron microscopy (TEM) images of the samples were recorded by 200 kV operating CM200, Philips unit. Fourier transform infrared (FTIR) spectroscopic

measurements were carried out on a Spectrum 65 spectrophotometer (Perkin Elmer). The spectra were collected at a resolution of 2 cm^{-1} and each spectrum was the average of thirty-two scans. UV-Vis absorption is performed on a Lambda 750 spectrometer, Perkin Elmer. Photoluminescence excitation (PLE) and emission (PL) measurements were performed using a Fluorolog-3 spectrofluorometer (Model: FL3-11, Horiba Jobin Yvon) equipped with 450 W Xenon flash lamp. The spectra were recorded after lamp intensity correction and spectral correction for PMT (photomultiplier tube) with slit width fixed at 1 nm. The 355 nm line from Nd:YAG pulsed laser (Innolas, Spitlight 600, Germany) having a pulse width 7 ns and repetition rate 10 Hz system was also used for PL (white light) measurements. The fluorescence decay time measurements of the different transitions were carried out at room temperature using the same Nd:YAG laser, and the data were acquired using a monochoromator (Spex, model: 340E, USA) equipped with PMT, an oscilloscope (analog digital scope-HM1507) and software SP107. The decay time was determined using the nonlinear least-squares fit method.

3. Results and Discussions

3.1 Structural characterization: X-ray diffraction, LeBail refinement, transmission electron microscopy and Fourier transform infrared measurement:

XRD patterns of $Y_{1.993}Dy_{0.001}Tm_{0.006}O_3$ phosphor sample, both as-synthesized sample and the sample annealed at 1200 ^oC for 2 h are shown in Fig. S1(a). Diffraction peaks for both the samples are consistent with the cubic bixbyte phase of Y_2O_3 (JCPDS no. 43-1036) with lattice parameter a= 10.6041 Å and space group *Ia*3 (206). There is no evidence of the peaks corresponding to doped lanthanide ions, or any other impurity; which confirms the synthesis of a phase pure material and also an effective doping of lanthanide ions (Dy^{3+} and Tm^{3+}) at Y^{3+} sites in cubic lattice. Further, the diffraction peaks in as-synthesized sample show a high value of full

width at half maxima (FWHM) and appears with low intensity. However, the intensity of the diffraction peaks are significantly improved for annealed sample and FWHM is also narrowed down. Both these results clearly indicate for an improvement in crystallinity as well as particle size for the annealed samples. This result is further supported with the TEM micrographs. TEM images of $Y_{1.993}Dy_{0.001}Tm_{0.006}O_3$ phosphor, both for as-synthesized sample and sample annealed at 1200 ^oC for 2 h, are shown in Fig. S1(b) and Fig. S1(c), respectively. The as-synthesized particles are nearly spherical, with average particle diameter 25 nm. However, in case of annealed samples, the particles are relatively agglomerated and show a rhomboid like geometry, some are spherical also. An inhomogeneous distribution of particles prevails with varied size and structure due to agglomeration of many crystallites to form larger lumps. The particle size can be estimated to be of the order of 80-100 nm.

Fig. 1(a) shows XRD patterns of $Y_{1.993}Dy_{0.001}Tm_{0.006}O_3$ phosphor doped with varying concentration of ZnO. Initially, when the concentration of ZnO is small (upto 6 mol% ZnO), no appreciable change in XRD pattern is seen and all the diffraction peaks can be easily indexed with Y_2O_3 phase. However, a very small shift (towards higher 2θ value) is noted in Fig. 1(b). This could easily be understood by taking into account the mismatch of ionic radius of Y^{3+} (0.90 Å) and Zn^{2+} (0.75 Å), which is more than 15%. Therefore, it is fairly expected that, Zn^{2+} ions will prefer to go into the interstitial sites. This will result in the increased cell volume of the cubic lattice giving rise to a shift towards higher 2θ value. A similar phenomenon has been widely reported in Li^+ ion doped different types of matrices including Y_2O_3 and summarized in a review article by our group.[20] It is to be noted here that, such interstitial occupancy by foreign ions appreciably changes crystal field symmetry around activator ions and, moreover to this, also causes evolution of vacancy in the material. Further, as the doping concentration of ZnO is

increased, few additional peaks appear along with earlier observed shift towards higher 2θ value. These additional peaks have been indexed well with wurtzite hexagonal structure of ZnO (JCPDS no. 36-1451). Fig. 1(c) shows the enlarged view of (100) peak of ZnO, which clearly demonstrates that, ZnO phase does not appear at low concentration upto 6 mol% while a clear evidence of phase formation can be seen for 10 mol % and above doping concentration.

In order to further index the low intensity XRD peaks, we determine the space group and unit cell parameters of the secondary phase by LeBail fitting of the XRD data using "FULLPROF" refinement program. The refinement was carried out using two phase model, for Y_2O_3 and ZnO (10 mol%) phases, the peak profiles were defined by Pseudo Voigt function and the background was described in terms of a six coefficient polynomial. A very good fit is observed by considering *Ia3* space group (of cubic cell) for Y_2O_3, and *P63m* space group (of hexagonal cell) for ZnO phase with the lattice parameter a= b= c= 10.6054(2) Å, and a= b= 3.2503(2), c= 5.2050(4) Å, respectively, (see Fig. 2a). The impurity peaks due to ZnO are expected due to the solubility limit of Zn^{2+} ion in the Y_2O_3 matrix. It is well known that as the amount of doping ion increases beyond the solubility limit, impurity phase can be obviously observed.[21] Further increase of ZnO content shows an improvement in the intensity of diffraction peaks due to ZnO phase, however, shift towards higher 2θ value remains constant. This also complements our claim that, initially up to a certain concentration Zn occupies the interstitials positions and beyond that, the dissolution limit of ZnO in Y_2O_3 phase appears. The exact solubility limit of Zn^{2+} in Y_2O_3 matrix or similar well established commercial hosts suitable for lanthanide ions would be an interesting problem for Crystallography and needs a detailed Rietveld refinement of XRD data, but beyond the scope of this study. Interestingly, beyond 10 mol% of ZnO doping, defect level induced emission of ZnO is observed in addition to the

characteristic peaks of lanthanide ions, which all together make it possible to get warm white light. The microstructure, however after ZnO addition, do not show any significant change except an increase in particle size which is in agreement with XRD data also. Some of the particles appear with size ~200 nm while some particles seem to be even higher in size length lying in the sub-micron range plausible due to large number of Zn^{2+} interstitial ions inside lattice, see Fig. 2(b).

To further investigate the presence of Zn^{2+} within the Y_2O_3 matrix, UV-Vis absorption has been performed in diffused reflectance mode for 3, 6, 10 and 40 mol% ZnO doped in Y_2O_3 matrix, shown in Fig. 3. Y_2O_3 has a single strong absorption band at ~210 nm and ZnO at 250-370 nm. For 3 and 6 mol% ZnO, it is clearly seen that there is a red shift in the absorption band of Y_2O_3 along with the significant appearance of band corresponding to ZnO absorption. It confirms the presence of ZnO into the host matrix. The red shift of the band at 210 nm is obviously due to increased cell volume, which happens due to the aforementioned assumption that Zn^{2+} would prefer to go into the interstitial site at low concentration (3 and 6%). Beyond which, at 10 mol% doping concentration, the red shift becomes negligible and it gets the original position as it is for pure Y_2O_3 itself, which suggests that interstitial occupation by Zn^{2+} ions remains no more effective at higher concentration, while, ZnO phase appears in addition with its characteristic absorption band. The ZnO absorption in UV region is significant, as under the 355 nm excitation, not only Tm^{3+} and Dy^{3+} excites but also ZnO would resonantly excite and give its defect emission, through radiative capture of electron hole pairs, along with characteristic rare earth emission. For 40 mol% and above only ZnO absorption is significantly observed.

To further explore the possibility of any coordination between Y^{3+} and Zn^{2+} ions to form composite system, FTIR measurements have been performed with pure Y_2O_3 and 10 mol% ZnO

doped Y_2O_3. Fig. S2 clearly reveals some vibrational interaction among the two ions. The various bands due to OH group (ν_{OH}, δ_{OH}), CO_3^{2-} group (ν_{CO}) and surface adsorbed NO_3^- group (ν_{NO}) appear more intense and sharper in the case of 10% ZnO than in pure Y_2O_3. This clearly indicates a rise in the number of surface defects created due to Zn^{2+} doping. These defects are responsible to enhance the red composition of the white light spectrum. Further, the characteristic peaks of Y-O vibration at 563 cm^{-1} reduces in the case 10% ZnO. Peak position, however, remains the same. This indicates some weak coordination between the two ions supporting the formation of a composite structure.

3.2 White light emission in $Y_{1.993}Dy_{0.001}Tm_{0.006}O_3$: Photoluminescence excitation, emission and energy transfer studies

PLE and PL spectra of Dy^{3+} and Tm^{3+} both, individually doped in Y_2O_3 matrix, are shown in Fig. 4(a) and Fig. 4(b), respectively. The excitation spectrum of Dy^{3+} (monitored for λ_{em}=571 nm) shows a broad band around 250 nm due to host absorption band (not shown in figure) and large number of sharp and discrete peaks spanned upto 450 nm due to characteristic excitation peaks of Dy^{3+}. The most intense excitation peak is obtained at around 355 nm resonant to $^6P_{7/2}$ level of Dy^{3+}. Similarly, the excitation spectrum of Tm^{3+} (monitored for λ_{em}= 452 nm) also shows the host absorption band and large number of sharp and discrete peaks due to characteristic excitation peaks of Tm^{3+} ion. Importantly, the most intense excitation peak for Tm^{3+} is also obtained at around 355 nm resonant to $^1D_2$ level of Tm^{3+}. The best excitation at around the same wavelength makes this lanthanide ion combination exceptional. Under 355 nm excitation, Dy^{3+} emanates in prominent yellow (at 571 nm) along with relatively weak emission in blue (485 nm), red (669 nm) and NIR (756 nm) region corresponding to the transitions $^4F_{9/2} \rightarrow {}^6H_{13/2}$, $^4F_{9/2} \rightarrow {}^6H_{15/2}$, $^4F_{9/2} \rightarrow {}^6H_{11/2}$ and $^4F_{9/2} \rightarrow {}^6H_{9/2}$, respectively. On the other hand, Tm^{3+} gives

intense peaks in blue region at 452 nm and 486 nm (relatively weak) attributed to $^1D_2 \rightarrow {}^3F_4$ and $^1G_4 \rightarrow {}^3H_6$ transitions, respectively. Additional weak bands in green (520-542 nm, corresponding to $^1D_2 \rightarrow {}^3H_5$ transition), red (~ 675 nm, due to $^1D_2 \rightarrow {}^3H_4$ transition) and NIR region (755-860 nm, due to $^1G_4 \rightarrow {}^3H_5/{}^3H_4 \rightarrow {}^3H_6$ transition) are also observed.[22-25] These two intense emission peaks in yellow and blue regions are complementary colors and hence, in a next attempt, they have been mixed in proper ratio (by varying the concentration of lanthanide ions in the matrix) to get a white light emission.

The concentration of Dy^{3+} has been optimized at 0.1 mol% at the outset and then the concentration of Tm^{3+} has been varied from 0.2 mol% to 0.8 mol%. The emission spectra are shown in Fig. 5(a). All the characteristic emission peaks corresponding to Tm^{3+} and Dy^{3+} remain present in the codoped samples also. Addition of Tm^{3+} in Dy^{3+} doped samples brings out two significant changes. Firstly, the characteristic blue emission appears which shows an enhancement in the emission intensity with an increase in doping concentration of Tm^{3+}ions and best intensity is attained for 0.6 mol% concentrations of Tm^{3+} ions, beyond which the intensity starts decreasing drastically due to the well known concentration quenching effect.[26] However, conversely, the emission intensity of the characteristic yellow transition of Dy^{3+} ion, and others too, decreases with increasing concentration of Tm^{3+} ions. This suggests for a possible energy transfer between Dy^{3+} and Tm^{3+} ions. The two levels $^4F_{9/2}$ (Dy^{3+}) and $^1G_4$ (Tm^{3+}) are of almost matching energy (~ 21000 cm^{-1}). Since the $^4F_{9/2}$ level of Dy^{3+} has a comparatively longer lifetime compared to $^1G_4$ level of Tm^{3+}, the energy exchange in these two levels is most likely to take place from Dy^{3+} to Tm^{3+}, as reported by Lakshaminarayana *et al* [13] also. The other direct channel of energy transfer is possible between levels $^6P_{7/2}$ (Dy^{3+}) and $^1D_2$ (Tm^{3+}).

The suggested energy transfer mechanism has been established further through time domain fluorescence measurements. Fig. 5 (b, c) shows decay behavior of transitions $^4F_{9/2}\rightarrow{}^6H_{13/2}$ (Dy^{3+}) and $^1G_4\rightarrow{}^3H_6$ (Tm^{3+}) both for singly and co-doped into the matrix. The profile has been fitted with first order exponential decay using the expression-

$$y = A \exp(-t/\tau) + y_0$$

where, y and y_0 are the intensities at time t and 0, respectively and τ is the lifetime of the emitting level and A is the fitting parameter. The decay lifetime of $^1G_4\rightarrow{}^3H_6$ transition of Tm^{3+} (acceptor) increases from 216 μs to 224 μs when co-doped with Dy^{3+}; while Dy^{3+} (donor) shows a decrease in lifetime from 605 μs to 391 μs for $^4F_{9/2}\rightarrow{}^6H_{13/2}$ transition when co-doped with Tm^{3+} ions. The transition $^4F_{9/2}\rightarrow{}^6H_{13/2}$ is regarded as a hypersensitive transition in Dy^{3+} and hence a significant rise time is also observed in this case, which also shows a decrease from 87.09 μs to 49.7 μs. This variation of lifetime between donor (Dy^{3+}) and acceptor (Tm^{3+}) ions clearly establishes a channel of energy transfer between them. The complete mechanism of energy transfer and different transitions are shown in the partial energy level diagram, shown in Fig. 6.

Now, if one looks on the CIE color coordinates of the different concentrations of Dy^{3+} and Tm^{3+}, the best result is obtained for $Y_{1.993}Dy_{0.001}Tm_{0.006}O_3$ (i.e. 0.1 mol% Dy^{3+} and 0.6 mol% Tm^{3+}) phosphor, see Fig. 5(d). The CIE coordinate obtained is (0.32, 0.34) which is quite close to a white light coordinate, see table 1. The correlated color temperature (CCT) for this white light is 6072 K which is very high and regarded as a cool white light , not very much suitable for warm white light applications. The color temperature herein has been calculated by McCAMY'S formula, which makes use of CIE color coordinates (x, y). According to this relation-

$CCT = 449n^3 + 3525n^2 + 6823.3n + 5520.33$; where, $n = (x - 0.3320) / (0.1858 - y)$.

3.3 Incorporation of ZnO in $Y_{1.993}Dy_{0.001}Tm_{0.006}O_3$: Defect level (DL) mediated red emission, correlated color temperature tuning and warm white light generation

In the next step, ZnO has been incorporated in the $Y_{1.993}Dy_{0.001}Tm_{0.006}O_3$ sample. As the concentration of ZnO is low enough no change/a very little change in CCT is attained. However, as the concentration of ZnO reaches 10% and beyond, CCT is appreciably affected. This could be understood from PL measurements. Two important new peaks are marked in the PL spectrum when ZnO concentration is 10 mol%, shown in Fig. 7, peaking at 635 nm and 706 nm. This evolution of red component is very important here to poise the spectral balance in getting warm white light. It arises mainly due to surplus surface oxygen interstitials/defects. Due to the small size, the surface to volume ratio increases. This generates a short range repulsive potential over the boundary region which hinders the motion of electrons. This potential uplift of the DL, due to oxygen on the surface, in relation to valence band give rise to the red emission through a transition between the defect states of Zn-O vacancy pair. Energy band diagram is shown in the inset of Fig. 7. It is also noteworthy that the common green deep DL which arises due to deficiency of oxygen is missing here because only one of the green or red emissions can be observed at a time [27]. The CIE for this spectrum is (0.38, 0.36) which lies in the white region of CIE plot. The CIE diagram showing a variation of color coordinate with a varying concentration of ZnO is shown in Fig. 8. The color temperature for this CIE coordinate is surprisingly improved to 3898 K, see table 1. This is superior in magnitude to be considered as warm white light. A digital photograph of this 10 mol% ZnO doped phosphor is shown in the inset of Fig. 8 which shows that the emission is very bright and efficient. Also, the performance of the phosphor is checked at the lamp operating temperature 150 ^{o}C and no significant change in PL is observed which is obvious as oxide matrices are thermally stable.

A plausible confusion may arise here as it is not continuous broad band which is usually the case with defect emission but structured and peak like as reported by Cai et al. and Verma et al. [28, 29]. To overcome this, we refer to the absorption data in Fig. 3 which confirms the change in the host absorption and the origin of defect level transition. The ZnO absorption is significant here at all concentration suggesting that, under the 355 nm excitation, not only Tm^{3+} and Dy^{3+} excites but also ZnO resonantly excites and give its defect emission, through radiative capture of electron hole pairs, along with characteristic rare earth emission. For 40 mol% and above only ZnO absorption is significantly observed and hence only ZnO emission dominated in the PL spectra. Also, in principle, red defect emission arises from deep defect states formed within the band gap. The large difference in energy from the band make it shielded from external perturbation (like thermal energy~ kT) and lattice influence. Therefore, these deep situated defect states recombine to give sharp peak like structured bands in place of continuous bands.

This DL mediated emission can be noticed even in 6 mol% concentration of ZnO, see inset to Fig. 7, whose intensity builds up with increasing concentration of ZnO. However, excess addition of ZnO content leads to a reduction in the emission intensity of lanthanide ions, and the emission from ZnO (both band edge and DL) itself dominates over the emission of lanthanide ions appreciably. Fig. 9 show the PL spectrum of the Y_2O_3-ZnO composite (40 mol% ZnO concentration) and the emission of lanthanide ions (Dy, Tm) doped in pure ZnO matrix. In case of 10 mol% concentration of ZnO, peaks due to lanthanide ions and ZnO both are clearly distinguishable and lanthanide emission is far better as compared to DL emission from ZnO, Fig. 7. However, for 40 mol% concentration, the situation is reversed and all the lanthanide peaks are superimposed over DL to give a broad emission lying in the range of 450-720 nm. Inset (I) of Fig. 9 shows the sharp peaks superimposed on broad band structure. But, the CIE coordinate

(0.34, 0.40) for this emission, deviates from ideal white light coordinates and moreover color temperature also deviate from the specified value and attains a value 5324 K, see table 1.

It is well known that ZnO is a direct band gap semiconductor, whereas, the f-f transitions of lanthanides are parity forbidden which are only partially relaxed when doped in a matrix. Therefore when both are excited simultaneously, there is a greater possibility of radiative recombination of excitons in ZnO as compared to the electronic transitions of lanthanide ions. Hence high concentration of ZnO resulted in its prominent intrinsic photoluminescence with a very weak lanthanide peaks superimposed over the broad emission which disappears as the concentration is further increased. The band edge emission of ZnO shows a red shift with increasing concentration of ZnO. This may be attributed to the increasing particle size with increase of ZnO concentration.

In, Dy^{3+} and Tm^{3+} co-doped pure ZnO sample emission intensity diminishes considerably and even white light emission is not achieved. It is well known that for semiconductor host materials there is only partial probability of lanthanide ion dissolution in the host matrix [30]. Also, the ionic radius of Zn^{2+} differs significantly from Dy^{3+} and Tm^{3+}. Consequently the possibility for lanthanide ions to substitute Zn^{2+} site or its coordination with Y^{3+} is not as effective as it is in case of Y^{3+} alone. The broad band emission in this case is expected mainly due to (DL) mediated emission of ZnO, which only appears in annealed samples. PL spectrum of the as-synthesized sample do not show this broad peak, see inset (II) to Fig. 9. Thus, ZnO as dopant acts as source of red spectral content which make it possible to tune the color temperature from a cool white light to a warm white light.

4. Conclusion

In conclusion, Tm^{3+} and Dy^{3+} co-doped Y_2O_3 nanophosphor have been synthesized. The phosphor with compositional formula $Y_{1.993}Dy_{0.001}Tm_{0.006}O_3$ yields a perfect cool white light with CIE coordinate (0.32, 0.34) and correlated color temperature (CCT) 6072 K. Further, ZnO has been co-doped into the matrix, which at lower concentration occupies interstitials position in form of Zn^{2+} and beyond 10 mol% concentration of ZnO, the dissolution limit of Zn^{2+} in Y_2O_3 matrix is reached and so ZnO phase also appears in the system making it an Y_2O_3-ZnO composite material. Due to this additional ZnO phase, defect level induced red spectral content is observed in addition, which tunes the color temperature from 6072 K (cool white light) to 3898 K (warm white light). This idea could be generalized in other potential host, particularly excitable through InGaN for indoor warm white ligh application.

Acknowledgement

S. K. Singh thankfully acknowledges the financial support by Department of Science and Technology (DST), New Delhi, India in the form of INSPIRE Faculty Award [IFA12-PH-21]. M. Rai is thankful to UGC, New Delhi for junior research fellowship (RFSMS). Thanks are also due to Dr. A. K. Singh (Department of Physics, UNAM, Mexico) for his help in the refinement of XRD data.

References:

1. S. Gandhi, K. Thandavan, B. J. Kwon, H. J. Woo, C. H. Kim, S. S. Yi, J. H. Jeong, D. S. Shin and K. Jang, *J. Mater. Chem. C*, 2014, **2**, 6630.
2. P. C. Shen, M. S. Lin and C. F. Lin, *Scientific Reports*, 2014, **4:5307**, 1.
3. E. H. Song, S. Ding, M. Wu, S. Ye, Z. T. Chen, Y. Y. Ma, and Q. Y. Zhang, *Opt. Mater. Express*, 2014, **4**, 1186.
4. K. Pavani, J. S. Kumar and L. R. Moorthy, *J. Am. Ceram. Soc.*, 2014, **97**, 1481.
5. C. C. Lin and R.S. Liu, *J. Phys. Chem. Lett.*, 2011, **2**, 1268.
6. H. A. Hoppe, *Angew. Chem.*, 2009, **48**, 3572.
7. M. R. Krames, O. B. Shchekin, R. M. Mach, G. O. Mueller, L. Zhou, G. Harbers and M. G. Craford, *J. Disp. Techn.*, 2007, **3**, 160.
8. C.H. Huang, T.M. Chen, W.R. Liu, Y.C. Chiu, Y.T. Yeh and S.M. Jang, *Appl. Mater. Interfaces*, 2010, **2**, 259.
9. X. Li, J. D. Budai, F. Liu, J. Y. Howe, J. Zhang, X. J. Wang, Z. Gu, C. Sun, R. S. Meltzer and Z. Pan, *Light Sci Appl*, 2013, **2**, 1.
10. L. Wu, Y. Zhang, M. Gui, P. Lu, L. Zhao, S. Tian, Y. Kong and J. J. Xu, *J. Mater. Chem.,* 2012, **22**, 6463.
11. C. H. Huang, W. R. Liu and T. M. Chen, *J. Phys. Chem. C*, 2010, **114**, 18698.
12. M. Shang, C. Li and J. Lin, *Chem. Soc. Rev.*, 2014, **43**, 1372.
13. G. Lakshminarayana, H. Yang and J. Qiu, *J. Solid State Chemistry*, 2009, **182,** 669.
14. X. Wua, Y. Liang, R. Chen, M. Liu and Z. Cheng, *Mat. Chem. Phys.*, 2011, **129**, 1058.
15. S. Liu, G. Zhao, X. Lin, H. Ying, J. Liu, J. Wang and G. Han, *J. Solid State Chem.,* 2008, **181**, 2725.

16. S. Vempati, J. Mitra and P. Dawson, *Nanoscale Res Lett.,* 2012, **7:470**, 1.

17. R. E. Marotti, J. A. Badán, E. Quagliata and E. A. Dalchiele, *Physica B*, 2007, **398,** 337.

18. L. Wu, Y. Wu, X. Pan and F. Kong, *Opt. Mater.*, 2006, **28**, 418.

19. M. Rai, K. Mishra, S. K. Singh, R. K. Verma and S. B. Rai. *Spectrochim. Acta, Part A*, 2012, **97**, 825.

20. A. K. Singh, S. K. Singh and S. B. Rai. *RSC Adv.***,** 2014, **4**, 27039.

21. Y. Q. Li, G. de With and H. T. Hintzen, *J. Solid State Chem.,* 2008, **181**, 515.

22. K. Mishra, S. K. Singh, A. K. Singh and S. B. Rai, *Mater. Res. Bull.,* 2012, **47**, 1339.

23. M. Jayasimhadri, B. V. Ratnam, K. Jang, H. S. Lee, B. Chen, S. S. Yi, J. H. Jeong and L. R. Moorthy, *J. Am. Ceram. Soc.,* 2010, **93**, 494.

24. N. K. Giri, S. K. Singh, D. K. Rai and S. B. Rai, *Appl. Phys. B*, 2010, **99**, 271.

25. A. Graeve, S. Verma, G.R. George, D.R. Brown and E.A. Lopez, *J. Am. Ceram. Soc.*, 2006, **89,** 926.

26. L. Laversenne, C. Goutaudier, Y. Guyot, M. T. C. Adad and G. Boulon, *J. Alloys Compd.,* 2002, **341**, 214.

27. S. A. Studenikinm, N. Golegu and M. Cocivera, *J. Appl. Phys.*, 1998, **84**, 2287.

28. J. H. Cai, G. Ni, G. He, Z. Y. Wu, *Physics Letters A*, 2008, **372,** 4104.

29. R. K. Verma, A. K. Singh, D. K. Rai, S. B. Rai, *Mat. Chem. Phys.*, 2012, **135**, 298.

30. F. Gu, S. W. Fen, M. K. Lu, G. J. Zhou, D. Xu and D. R. Yuan, *Langmuir*, 2004, **20**, 3528.

Table 1 A comparative study of CIE and CCT values for different samples. The missing CCT value indicates the deviation from white light region.

Sample	**CIE coordinate**	**CCT (K)**
$Y_{1.997}Dy_{0.001}Tm_{0.002}O_3$	(0.38, 0.42)	……
$Y_{1.995}Dy_{0.001}Tm_{0.004}O_3$	(0.37, 0.40)	……
$Y_{1.993}Dy_{0.001}Tm_{0.006}O_3$	(0.32, 0.34)	6072
$Y_{1.991}Dy_{0.001}Tm_{0.008}O_3$	(0.29, 0.29)	8842
$Y_{1.993}Dy_{0.001}Tm_{0.006}O_3$+ 10 mol% ZnO	(0.38, 0.36)	3898
$Y_{1.993}Dy_{0.001}Tm_{0.006}O_3$+ 40 mol% ZnO	(0.34, 0.40)	5324
ZnO+0.1 mol% Dy+0.6mol% Tm	(0.36, 0.43)	------

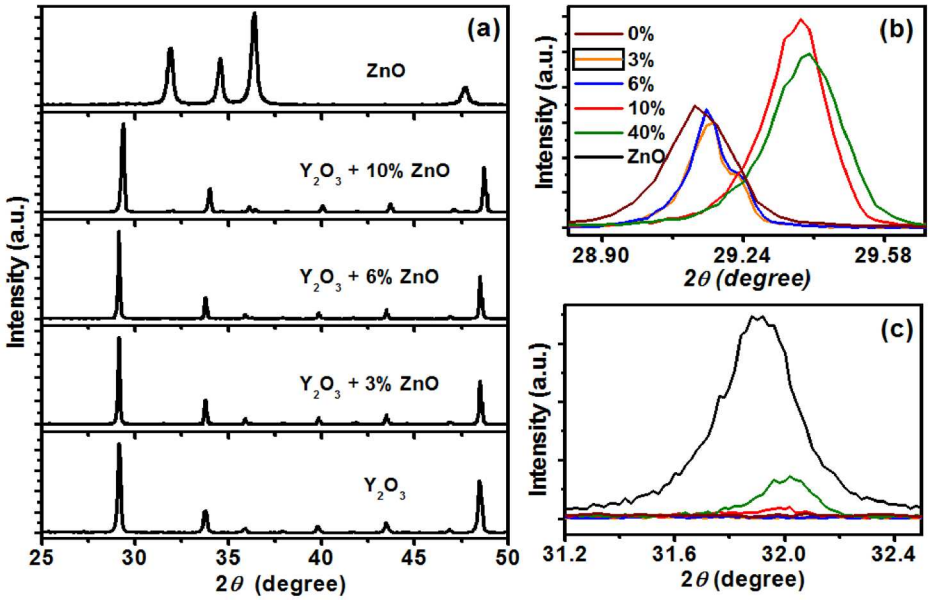

Fig. 1 (a) X-ray diffraction pattern of Y_2O_3, Y_2O_3-ZnO composite and pure ZnO; (b) enlarged view showing 2θ shift in the dominent peak at 29.12^0 of Y_2O_3 with addition of ZnO content; and (c) Appearance of diffraction peak due to ZnO.

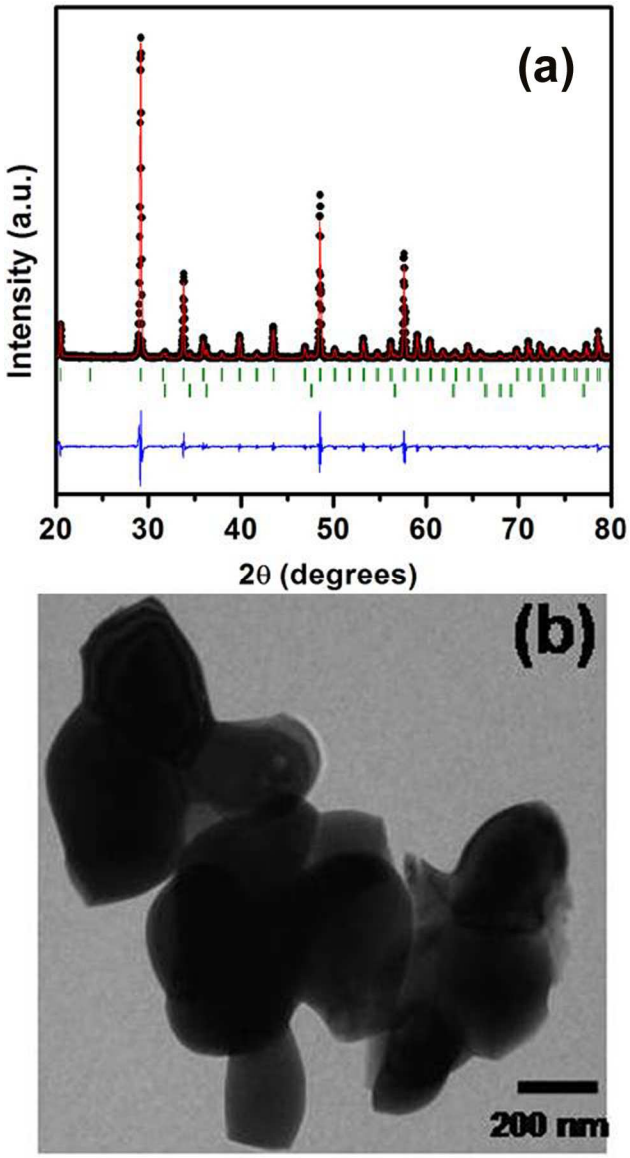

Figure 2 (a) Observed (dots), calculated (continuous line), and difference (bottom line) profiles obtained after Le Bail fit for Y_2O_3-ZnO phosphor using *Ia3* space group (of cubic cell) for Y_2O_3, and *P*63m space group (of hexagonal cell) for ZnO phases. Vertical tick marks above the difference plot show the positions of the Bragg peaks. (b) Transmission electron microscopy (TEM) image of Y_2O_3-ZnO composite.

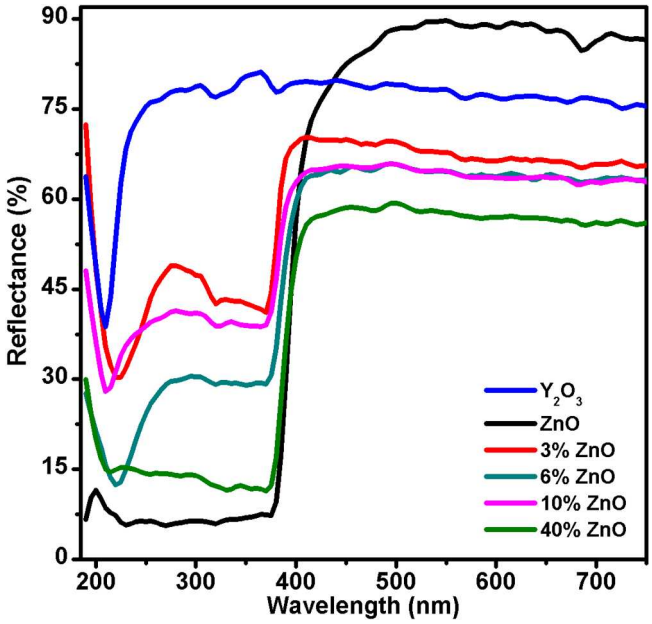

Fig. 3 UV-Visible absorption spectra of pure Y_2O_3, ZnO and composite of both at different concentration of ZnO

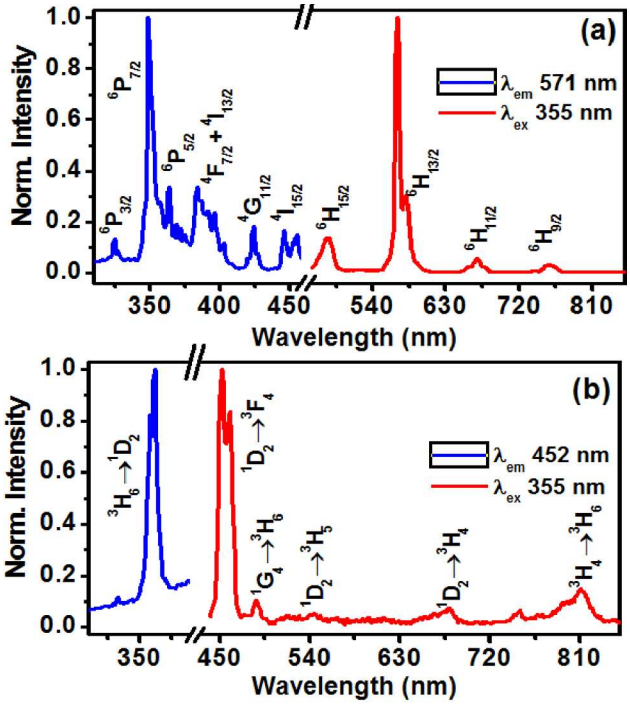

Fig. 4 Photoluminescence excitation (PLE) and emission (PL) measurement of (a) Dy^{3+} doped Y_2O_3, λ_{em} 571 nm and λ_{ex} 355 nm ; (b) Tm^{3+} doped Y_2O_3, λ_{em} 452 nm and λ_{ex} 355 nm.

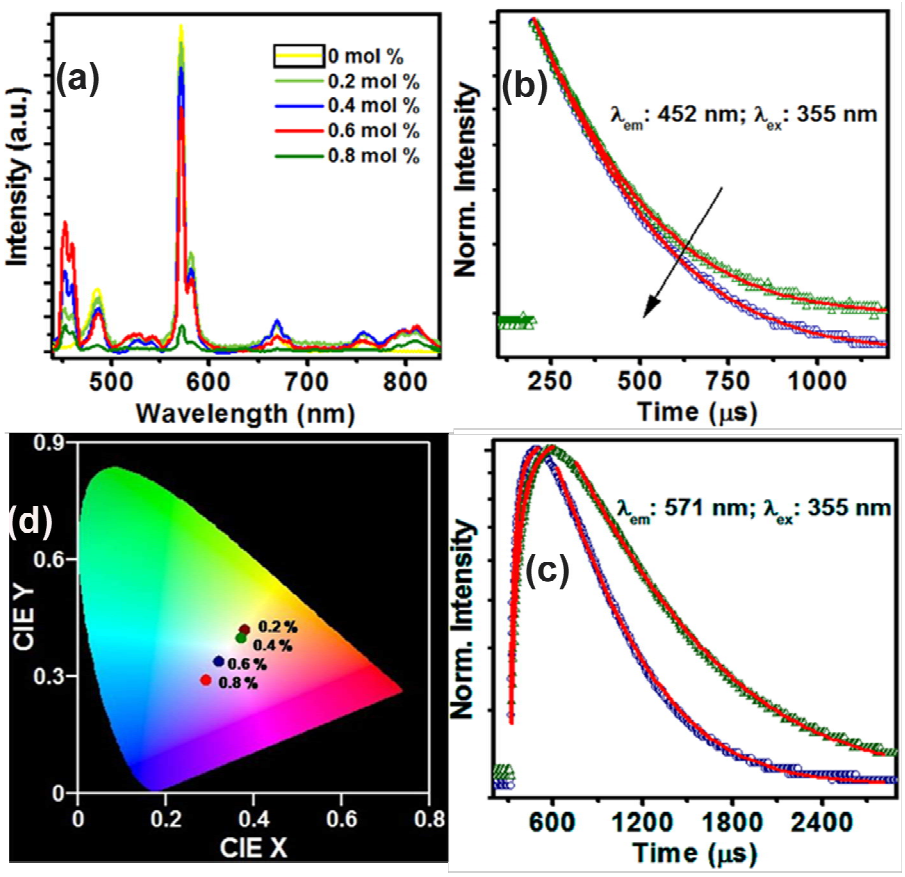

Fig. 5 (a) PL of Dy^{3+} doped Y_2O_3 with increasing Tm^{3+} concentration; (b) Decay curves showing an increase in lifetime of $^1G_4$ level of Tm^{3+} with codoping of Dy^{3+} (blue profile); and (c) A decrease in lifetime of $^4F_{9/2}$ level of Dy^{3+} with codoping of Tm^{3+} and (d) CIE plot with Tm^{3+} concentration in the codoped sample

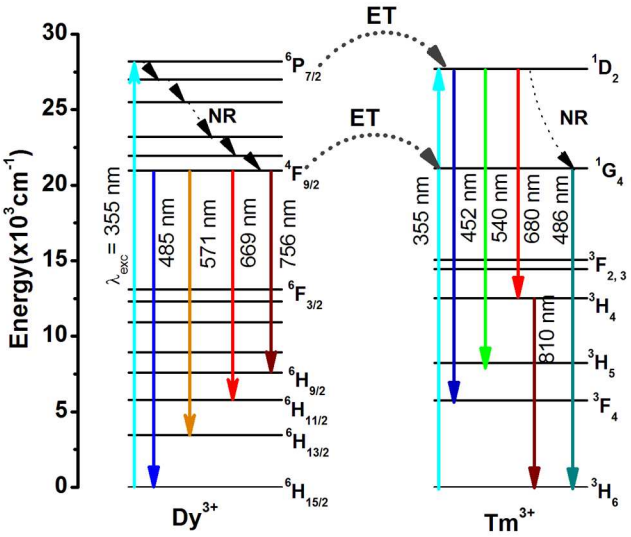

Fig. 6 Partial energy level scheme showing various transitions under 355 nm excitation and the possible channels of energy transfer (ET); NR stands for non radiative relaxations

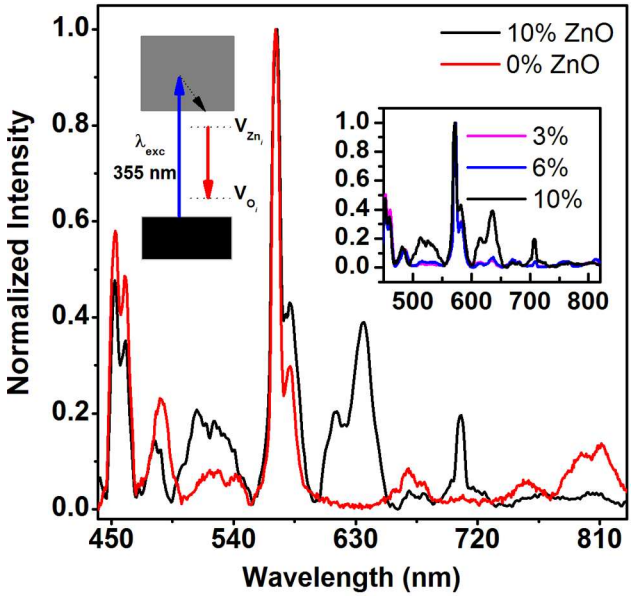

Fig. 7 Normalized emission spectrum of undoped and 10 mol% codoped ZnO in $Y_{1.993}Dy_{0.001}Tm_{0.006}O_3$ phosphor; left inset shows the origination of red emission from the defect levels of ZnO; right inset shows a steady increase in the defect emission intensity with increasing ZnO content.

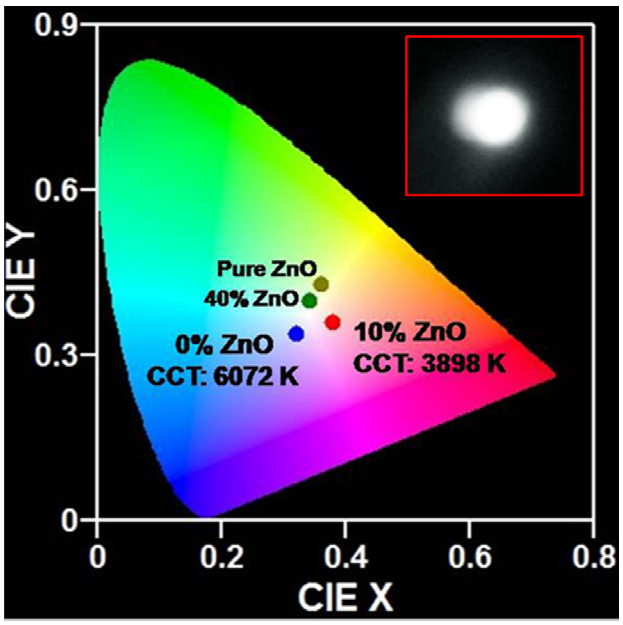

Fig. 8 CIE plot of $Y_{1.993}Dy_{0.001}Tm_{0.006}O_3$ and the samples doped with 10 and 40 mol% ZnO, and Tm^{3+}/Dy^{3+} doped in pure ZnO. Inset shows the digital image of the phosphor corresponding to 10 mol% ZnO.

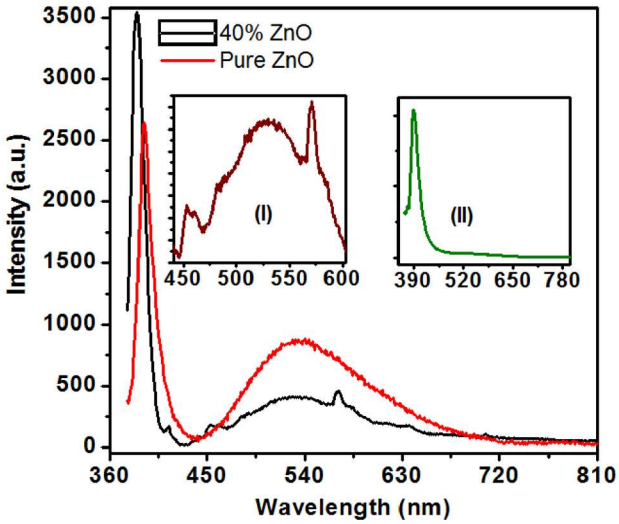

Fig. 9 PL of 40 mol% doped $Y_{1.993}Dy_{0.001}Tm_{0.006}O_3$ and Tm^{3+}/Dy^{3+} co-doped pure ZnO under 355 nm excitation; Inset I shows Tm^{3+}, Dy^{3+} emission superimposed over the defect level of ZnO; Inset II shows only band edge emission in as synthesized ZnO phosphor, no signature of defect level emission is observed.

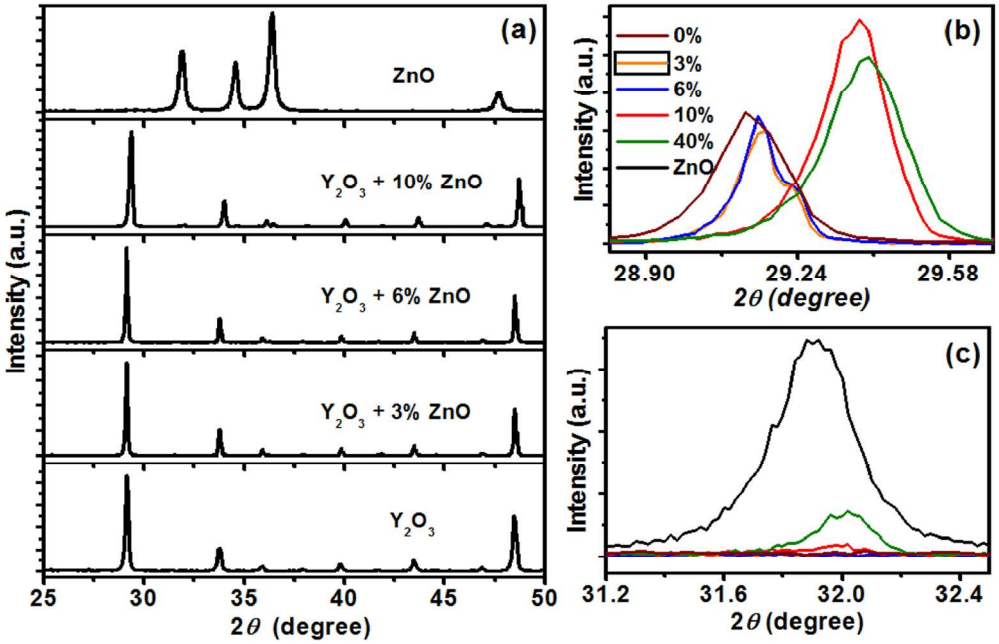

Fig. 1 (a) X-ray diffraction pattern of Y2O3, Y2O3-ZnO composite and pure ZnO; (b) enlarged view showing 2θ shift in the dominent peak at 29.12^0 of Y2O3 with addition of ZnO content; and (c) Appearance of diffraction peak due to ZnO.

123x80mm (300 x 300 DPI)

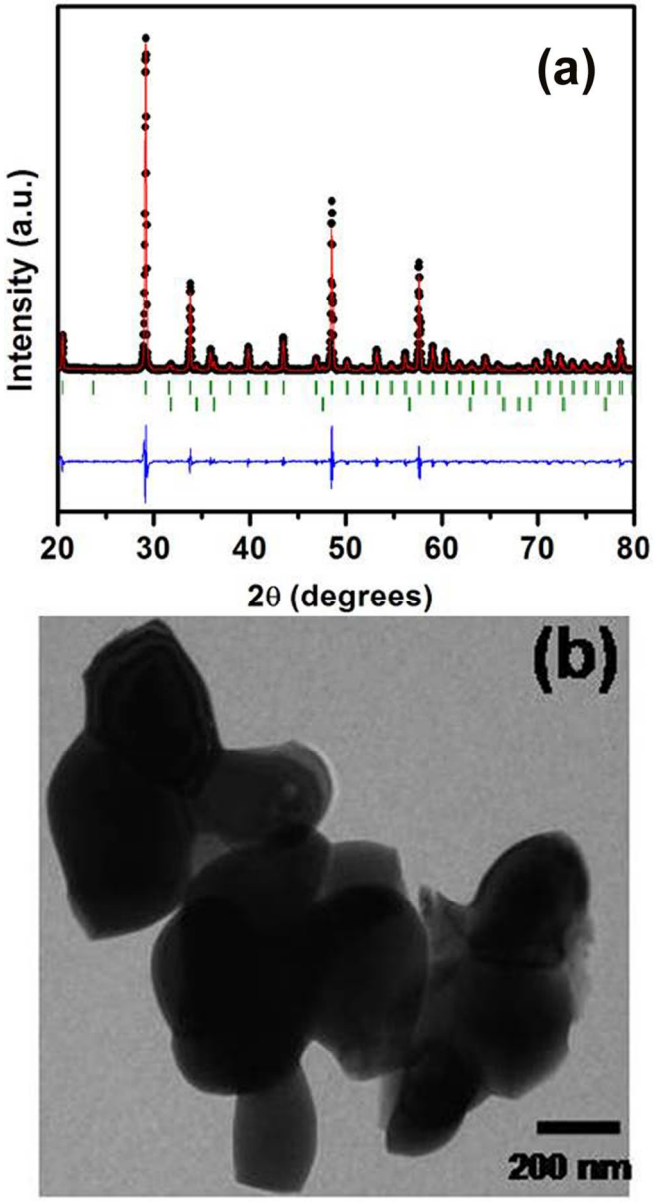

Figure 2 (a) Observed (dots), calculated (continuous line), and difference (bottom line) profiles obtained after Le Bail fit for Y2O3-ZnO phosphor using Ia3 space group (of cubic cell) for Y2O3, and P63m space group (of hexagonal cell) for ZnO phases. Vertical tick marks above the difference plot show the positions of the Bragg peaks. (b) Transmission electron microscopy (TEM) image of Y2O3-ZnO composite.
82x152mm (300 x 300 DPI)

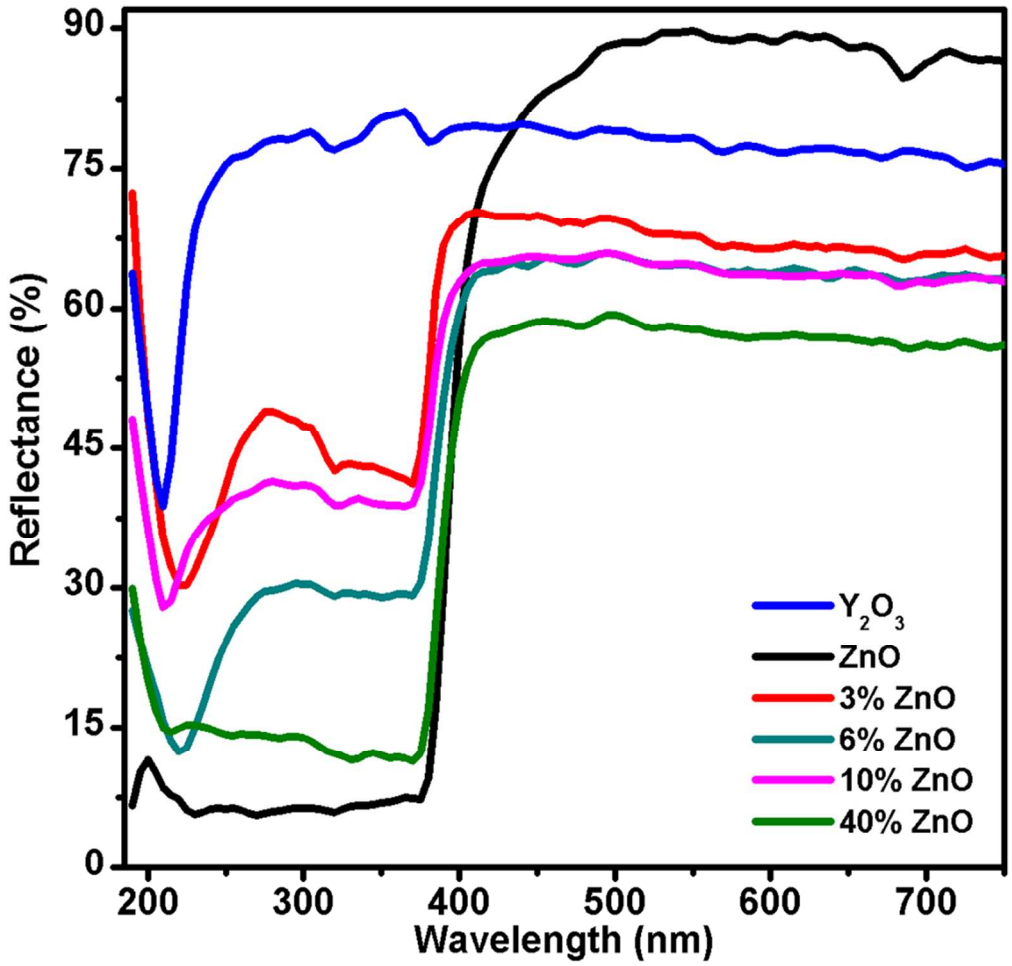

Fig. 3 UV-Visible absorption spectra of pure Y2O3, ZnO and composite of both at different concentration of ZnO
85x81mm (300 x 300 DPI)

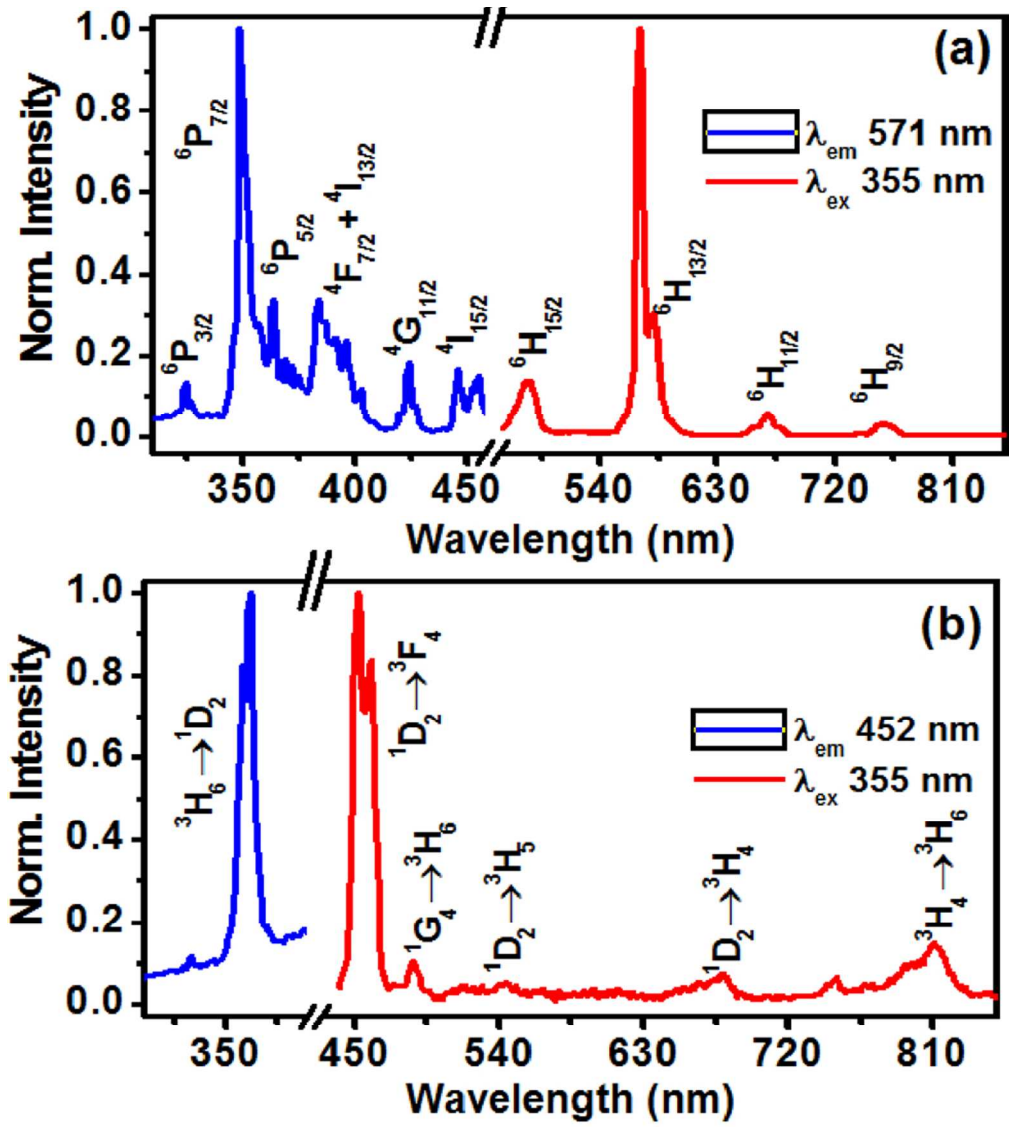

Fig. 4 Photoluminescence excitation (PLE) and emission (PL) measurement of (a) Dy3+ doped Y2O3, λem 571 nm and λex 355 nm ; (b) Tm3+ doped Y2O3, λem 452 nm and λex 355 nm.

82x92mm (300 x 300 DPI)

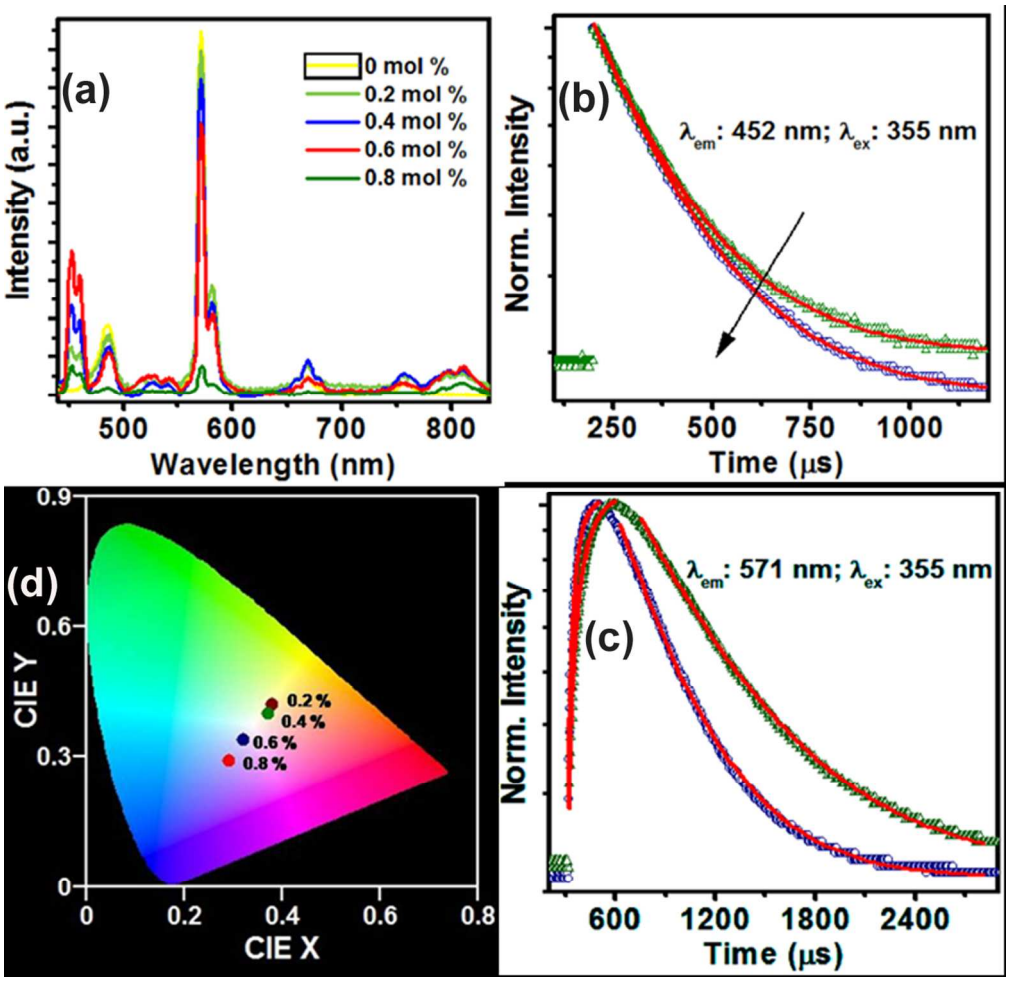

Fig. 5 (a) PL of Dy3+ doped Y2O3 with increasing Tm3+ concentration; (b) Decay curves showing an increase in lifetime of 1G4 level of Tm3+ with codoping of Dy3+ (blue profile); and (c) A decrease in lifetime of 4F9/2 level of Dy3+ with codoping of Tm3+ and (d) CIE plot with Tm3+ concentration in the codoped sample
118x115mm (300 x 300 DPI)

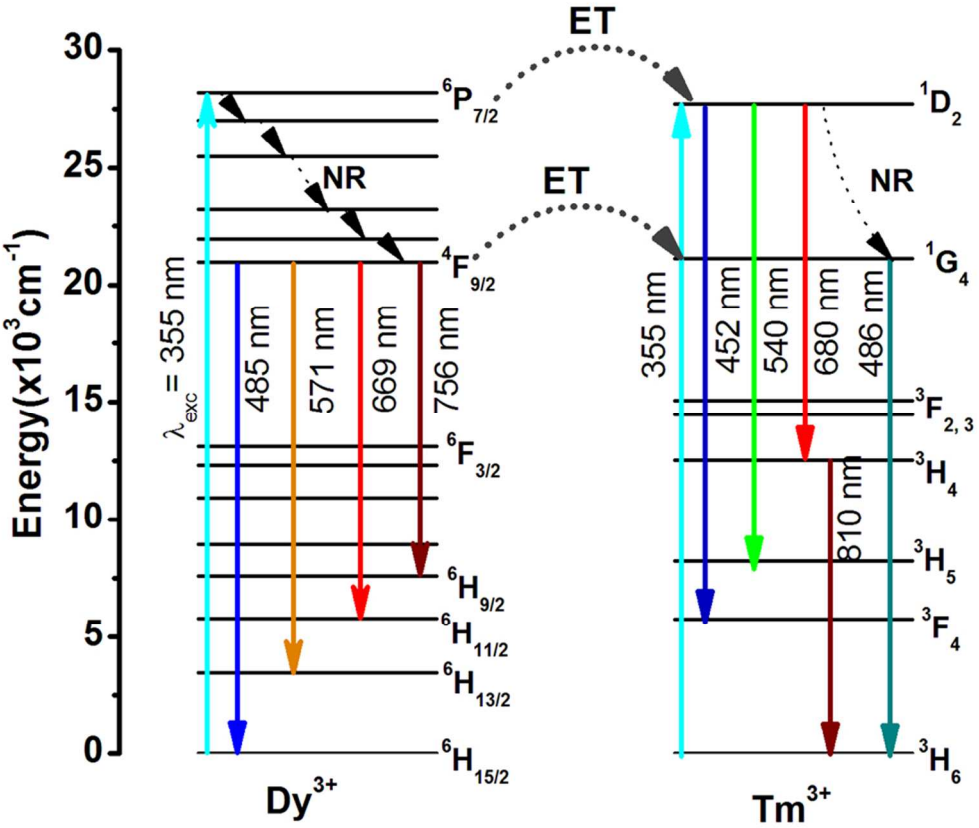

Fig. 6 Partial energy level scheme showing various transitions under 355 nm excitation and the possible channels of energy transfer (ET); NR stands for non radiative relaxations
85x71mm (300 x 300 DPI)

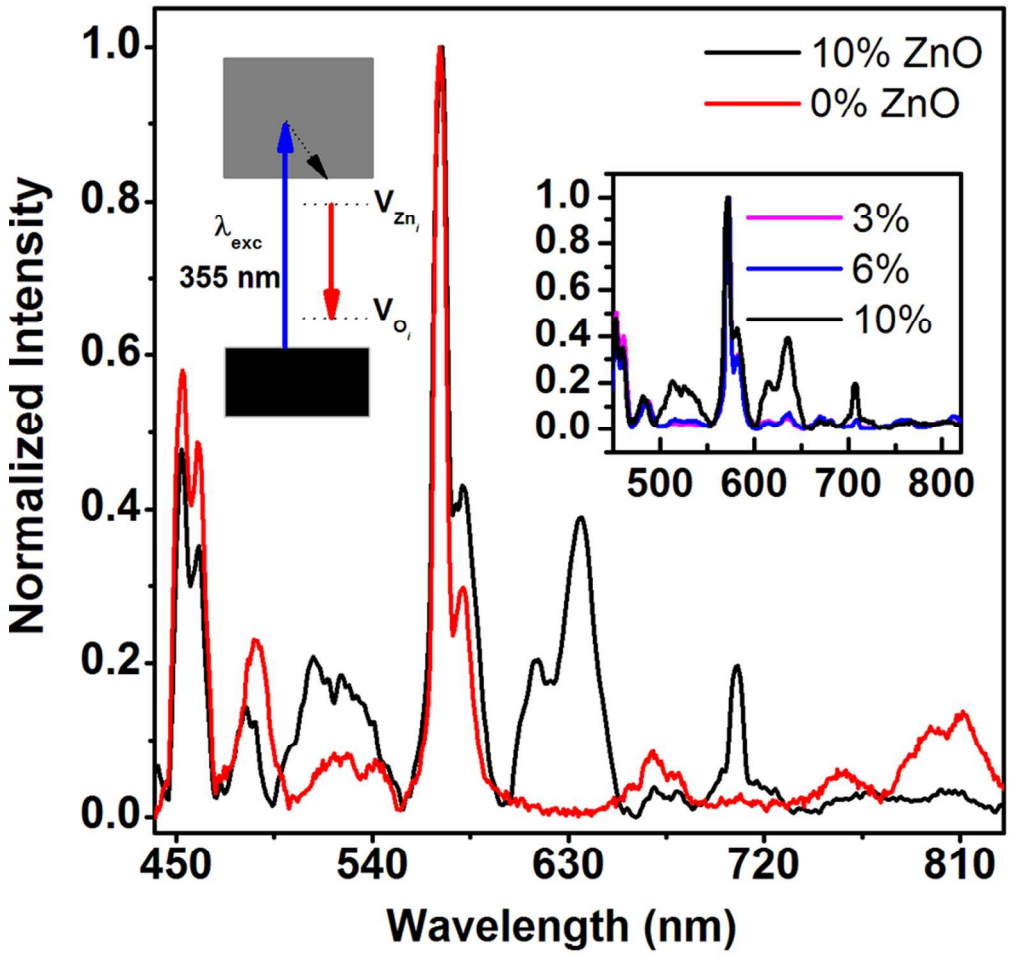

Fig. 7 Normalized emission spectrum of undoped and 10 mol% codoped ZnO in Y1.993Dy0.001Tm0.006O3 phosphor; left inset shows the origination of red emission from the defect levels of ZnO; right inset shows a steady increase in the defect emission intensity with increasing ZnO content.

82x78mm (300 x 300 DPI)

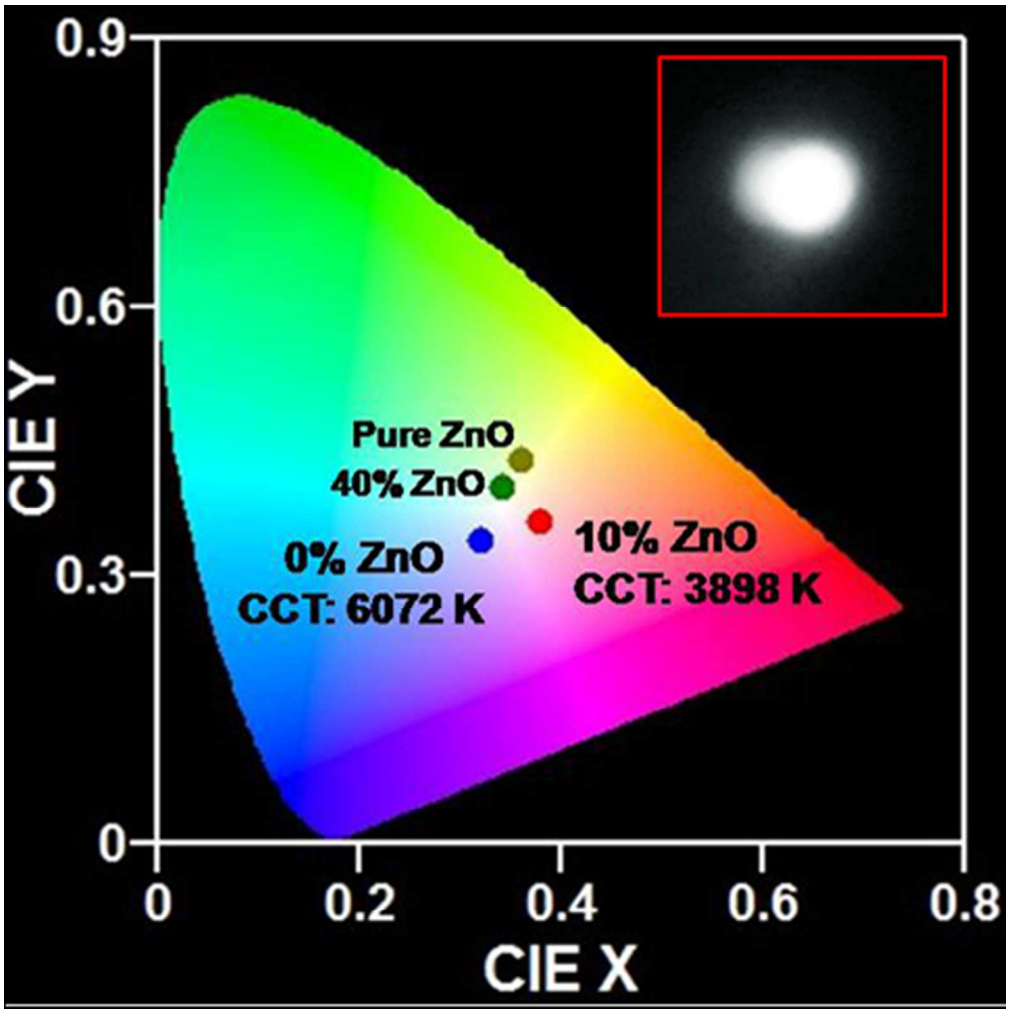

Fig. 8 CIE plot of Y1.993Dy0.001Tm0.006O3 and the samples doped with 10 and 40 mol% ZnO, and Tm3+/Dy3+ doped in pure ZnO. Inset shows the digital image of the phosphor corresponding to 10 mol% ZnO.
81x81mm (300 x 300 DPI)

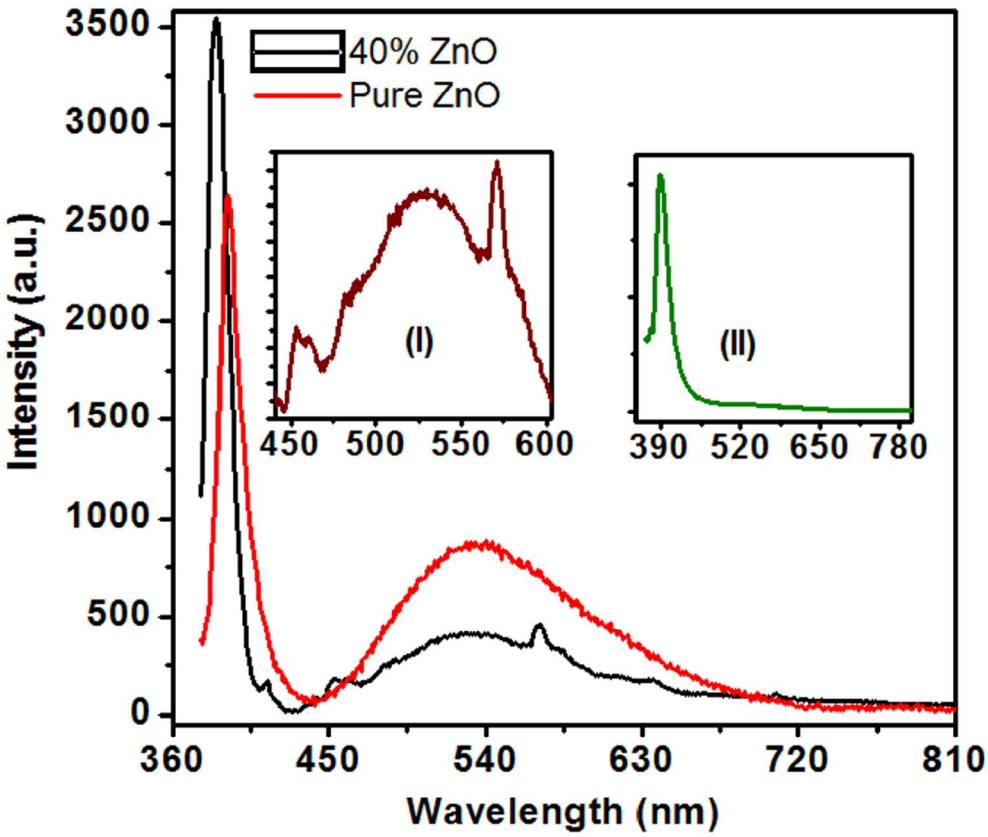

Fig. 9 PL of 40 mol% doped Y1.993Dy0.001Tm0.006O3 and Tm3+/Dy3+ co-doped pure ZnO under 355 nm excitation; Inset I shows Tm3+, Dy3+ emission superimposed over the defect level of ZnO; Inset II shows only band edge emission in as synthesized ZnO phosphor, no signature of defect level emission is observed.
82x70mm (300 x 300 DPI)